CrossMark

A Waveguide-Coupled Surface Plasmon Resonance Sensor Using an Au-MgF$_2$-Au Structure

Pengfei Zhang [1,2] · Le Liu [3] · Yonghong He [2] · Xiaoxia Chen [4] · Kaijie Ma [5] · Dong Wei [1]

Abstract

We describe an Au-MgF$_2$-Au trilayered waveguide-coupled surface plasmon resonance (WCSPR) sensor in this article. The characteristics of this sensing structure are compared with those of the conventional single-layered gold surface plasmon resonance (SPR) sensor theoretically and experimentally. The experiment results show that WCSPR can provide not only seven times smaller refractive index resolution in the bulk sensing application but also more accurate measurement results for the biomolecular interaction analysis than the conventional single-layered gold SPR. What's more, this high-resolution sensor is easy to build and not sensitive to film thickness variations. The Au-MgF$_2$-Au trilayered WCSPR may provide a simple and convenient chip-based strategy for performance enhancement of SPR sensors without varying the hardware and software of measurement instruments.

Keywords Surface plasmon resonance · Waveguide-coupled surface plasmon resonance · Residual analysis · Biomolecular interaction analysis

Introduction

Surface plasmon resonance (SPR) is an optical sensing approach offering the advantages of high sensitivity and label free [1–3]. Combined with the immobilized biorecognition elements, the SPR sensor can become a powerful tool for biomolecular interaction analysis [4–8]. Over the decades, many efforts have been made to further improve the sensing performance of this sensitive analytical tool including the polarization interference interrogation [9], light source optimization [10], resonance wavelength optimization [11], weak-value amplification of SPR signals [12], signal enhancement with plasmonic nanoparticles [13], chemistry-based signal amplification [14], and chip-based strategy [8, 14]. The chip-based strategy is expected to be versatile and cost-effective in practical applications, and can be readily realized without varying the hardware and software of the SPR instruments, so it has drawn great attentions in the SPR method development and there have been many innovations presented over the past couple of years. One important chip-based strategy is improvement of sensor chip structure, which mainly includes the plasmonic nanorod metamaterials [15], utilizing the transparent material as adherent layer [16], multilayer metallic structures [17], long-range SPR [18, 19], plasmon waveguide resonance [20–25], and waveguide-coupled surface plasmon resonance (WCSPR) [14, 26].

WCSPR is usually constructed by inserting a dielectric waveguide layer between two metal layers [27]. WCSPR can not only provide superior sensing performance but also permit more resonance modes for extended applications than the conventional single-layered SPR [28–31]. It has been reported that the material of waveguide layer plays a significant role in the coupling of SPR and waveguide resonance [32]. Different materials including optical polymer [28], ZnS-SiO$_2$

✉ Pengfei Zhang
pfz@mail.ustc.edu.cn

1   Beijing Scientific Instrument Research and Development Center, Chinese Academy of Sciences, Beijing 100190, China

2   Shenzhen Key Laboratory for Minimal Invasive Medical Technologies, Institute of Optical Imaging and Sensing, Graduate School at Shenzhen, Tsinghua University, Shenzhen 518055, China

3   Institute of Green Chemistry and Energy, Graduate School at Shenzhen, Tsinghua University, Shenzhen 518055, China

4   Department of Ophthalmology, Xin Hua Hospital Affiliated to Shanghai JiaoTong University School of Medicine, Shanghai 200092, China

5   Department of Physics, Tsinghua University, Beijing 100084, China

[33, 34], SiO$_2$ [35], and Hafnium dioxide [36] have used to construct the WCSPR sensor chip.

In this article, we presented an Au-MgF$_2$-Au trilayered WCSPR sensing structure. The MgF$_2$ has low RI value so that the high refractive index (RI) contrast can be achieved between it and the high RI prism, which is commonly used in the conventional single-layered gold SPR sensors [8]. It has been pointed out that better WCSPR sensor performance can be achieved with higher RI contrast between the prism and waveguide layer [32]. Besides, the MgF$_2$ layer is easy to prepare and needs no adhesive layer with Au film with common vacuum evaporation coating [37]. The characteristics of Au-MgF$_2$-Au trilayered WCSPR sensing structure are compared with those of the conventional single-layered gold SPR sensor theoretically and experimentally to demonstrate that it can achieve better performance without varying the hardware and software of the common SPR instruments.

Materials and Methods

Reagents

The materials (Au, Cr, MgF$_2$) used for vacuum coating were acquired with 99.99% purity from China New Metal Materials Technology Co., Ltd. (Beijing, China). Polished optical glass substrates and prisms were purchased from Fuzhou Jiuyi Optics Co., Ltd. (China). KH$_2$PO$_4$, Na$_2$HPO$_4$, KCl, and NaCl are purchased from Alfa-Aesar (USA). Glucose, 3-mercaptopropionic acid (MPA), N-hydroxysuccinimide (NHS), and 1-ethyl-3-(3-dimethylaminopropyl) carbodiimide hydrochloride (EDC) are purchased from the Aladdin (China), in molecular biology grade or higher. Protein A and human IgG were purchased from Tianze Biotechnology (Guangzhou, China). Milli-Q water (18.2 MΩ cm, Millipore Corp., USA) was used throughout the experiments. All the other organic solvents and chemical reagents were purchased from Shenzhen Tianxiang Huabo Co., Ltd. (China), and were used as received without further purification. The composition of PBS buffer is 1.4 mM KH$_2$PO$_4$, 8 mM Na$_2$HPO$_4$, 2.7 mM KCl, 137 mM NaCl, pH 7.4 at 25 °C. The PBS$_{BSA}$ buffer is prepared by adding 1000 μg/mL BSA to PBS. The composition of EDC/NHS solution is 20 mM EDC and 5 mM NHS. The MPA solution is prepared by adding 100 mM MPA to ethanol. The protein A and IgG solution is prepared by adding protein A and IgG to the PBS buffer.

Design Optimization

The SPR and WCSPR sensor modules were carried out using the Kretschmann prism coupling technique as shown in Fig. 1a. Three nanometers of Cr film ($n = 3.44 + 4.34i$) was deposited on SF4 optical glass substrate ($n = 1.75$) as the

adhesive layer. Then, an Au film ($n = 0.13 + 3.65i$) was deposited on the coated substrate to construct the SPR sensor chip. An Au film ($n = 0.13 + 3.65i$) as upper Au film, a MgF$_2$ film ($n = 1.38$) as waveguide layer, and another Au film as lower Au film ($n = 0.13 + 3.65i$) were sequentially deposited on the coated substrate to construct the WCSPR sensor chip. The material RI was referred as n. The sensor chips were placed on the polished optical glass prisms with the RI matching oil (Cargille) to implement the sensor modules.

The SPR sensor performance can be theoretically predicted using the combined sensitivity factor (CSF) function, which was inversely related to sensor resolution and shown as follows:

$$\text{CSF}_{\text{bulk}} = S_{\text{bulk}} \times \frac{R_{\max} - R_{\min}}{\text{FWHM}}, S_{\text{bulk}} = \frac{\partial \theta}{\partial n} \qquad (1)$$

$$\text{CSF}_{\text{surf}} = S_{\text{surf}} \times \frac{R_{\max} - R_{\min}}{\text{FWHM}}, S_{\text{surf}} = \frac{\partial \theta}{\partial d} \qquad (2)$$

where $R_{\max}$ and $R_{\min}$ are the maximum and minimum normalized reflectance; FWHM is the full width at half maximum; θ is the resonance angle; n and d are the bulk RI and binding layer thickness; S_{bulk} and S_{surf} are the bulk sensitivity factor in degree angle/refractive index unit (RIU) and surface sensitivity factor in degree angle/nanometer thickness, respectively; and CSF_{bulk} and CSF_{surf} are the CSF defined for bulk and surface sensing applications, respectively [38, 39]. Based on the theoretical simulation algorithm [39], the correlations of CSF_{bulk} and CSF_{surf} with film thicknesses were calculated as shown in Fig. 1b for SPR and WCSPR sensors. It can be seen that both CSF_{bulk} and CSF_{surf} vary along with the sensing film thicknesses in SPR and WCSPR sensors. Fortunately, both the CSF_{bulk} and CSF_{surf} stay at a high level within about 15% of the optimization film thickness in SPR and WCSPR sensors. This indicated that the WCSPR sensor is less sensitive to the film thickness fluctuations around the optimization value as well as the SPR sensor, which is of great use in the practical applications. It has been reported that continuous MgF$_2$ film with thickness of several hundred nanometers could be prepared using the vacuum evaporation coating technique [37], and the continuous Au film with thickness of over 40 nm could be prepared using the direct current magnetron sputtering technique [37, 40]. Considering these, 650 nm was employed as the thickness of MgF$_2$ waveguide layer, and 40 nm was employed as the lower Au film thickness in WCSPR sensor to balance the sensor performances in bulk and surface sensing applications. The upper Au film thicknesses for WCSPR sensor would be designated after determining the smallest thickness of continuous Au film that could be provided by the direct current magnetron sputtering technique used in this study; 60 nm was employed as the thickness of Au film in SPR sensor.
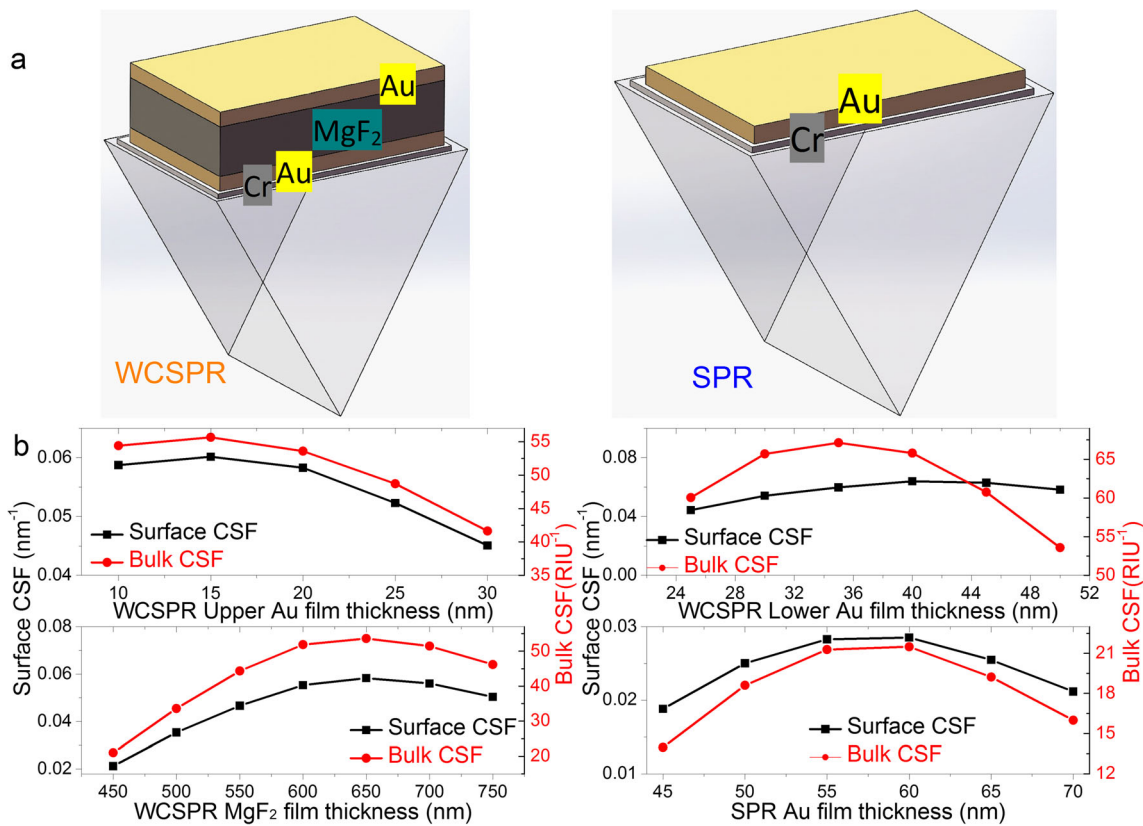
Fig. 1 **a** Schematic representations of SPR and WCSPR sensor modules. **b** Correlations of combined sensitivity factors for surface and bulk sensing applications with the film thicknesses in SPR and WCSPR sensors

Fabrication of Thin Au Film

A high-vacuum magnetron sputtering system (TA14-01D, Tengao Machinery Manufacturing Co., Ltd., Shenyang, China) was employed to prepare the thin Au film. The film thickness was controlled by a quartz crystal oscillator thickness monitor. Polished SF4 glass substrates are ultrasonically cleaned in a solution consisting of ethanol and diethyl ether in 1:1 ratio, then rinsed with deionized water, and dried with nitrogen. The substrate is heated and maintained at 400 °C and given a negative bias voltage during the coating process. The substrate heating decreases the gas molecules absorbed on the surface and accelerates the movement of the metallic particles on the surface for even film growth. The negative bias voltage makes the gas ion impact the film surface to average the film growth speed further and removes the weakly bound metallic particles and the absorbed gas molecules.

The Au films with the thicknesses of 15 and 20 nm were deposited on polished SF4 glass substrates and characterized using an analytical scanning electron microscope (SEM, KYKY-EM8000F, KYKY Technology Co. Ltd., China) equipped with the energy-dispersive spectrometer (EDS, TeamTM, EDAX company, USA), and the corresponding EDS maps were shown in Fig. 2a. It can be seen that Au element showed uniform surface distributions, which

indicated that the thin Au film can be prepared with the magnetron sputtering technique. Then, the detailed surface topographies were inspected using the image mixing the secondary electron and backscattered electron signals achieved by a Schottky field emission SEM (Quanta 250F, FEI, USA) as shown in Fig. 2b. It can be seen that apparent pores and cracks existed on the surface of 15 nm Au film, which may have negative effect on the sensor performance in imaging applications. Considering the aforementioned factors, 20 nm was designated to be the upper Au film thickness in a WCSPR sensor.

Experimental Setup

A one-dimensional SPR imaging system was constructed based on the angle interrogation for this study as shown in Fig. 3. In this system, the light-emitting diode (A) combined with the bandpass filter (E, center wavelength 632.8 nm, bandwidth 10 nm, Thorlabs) is used to acquire the desired incident wavelength, which has been demonstrated to be an excellent choice to suppress the speckle effect in the angular SPR imaging system [10]. A × 25 objective lens (B) was used to focus the light emitted by a red light-emitting diode with an electric power of 3 W on a pinhole (C). The light beam was collimated using a convex lenses (D) and p-polarized by a

Fig. 2 **a** EDS maps of 15 and 20 nm Au films. **b** Surface micrographs of 15 and 20 nm Au films
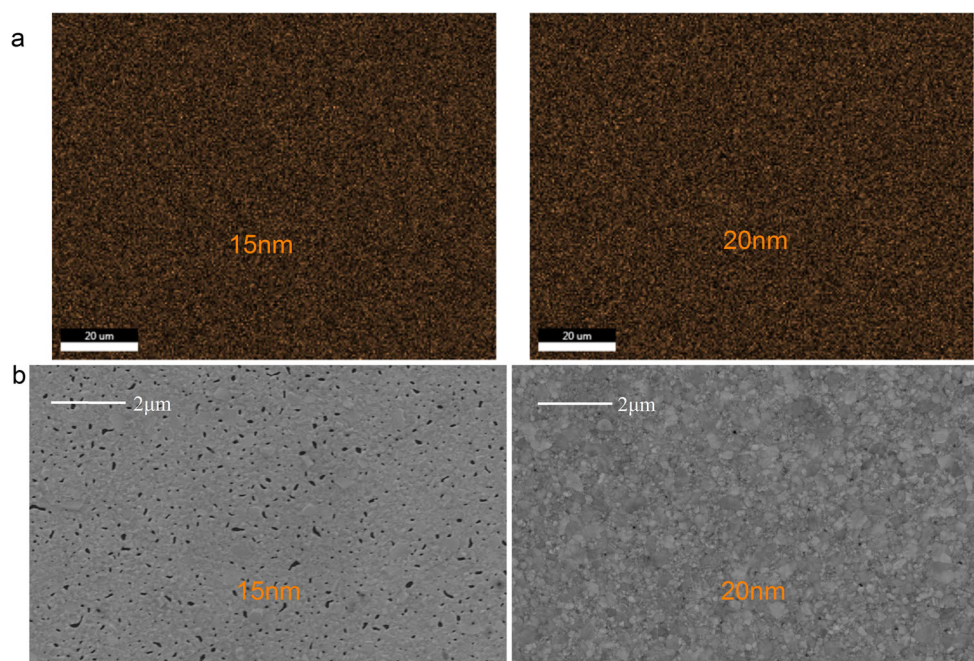
linear glass polarizer (F). An aperture (G) was used for a rectangular spot. After passing through a cylindrical lens (H) with vertical axis of symmetry, the light was focused to a line to construct an imaging channel. The SPR or WCSPR sensor module (I) was configured in the Kretschmann manner and a two-channel polymethyl methacrylate fluidic system (FS, $10 \times 2 \times 2$ mm^3, 40 μL), where one channel played the role of detection channel and the other played the role of reference channel to discriminate the nonspecific absorption in biomolecular interaction analysis, was attached to the sensor chip for sample delivery. The reflection light was collimated by another cylindrical lens (J) with vertical axis of symmetry and recorded by a charge coupled device (K, 3032×2018 pixels, 7.8-μm pixel size, ICX413AQ, Sony) for further data analysis in a personal computer. A temperature control system based
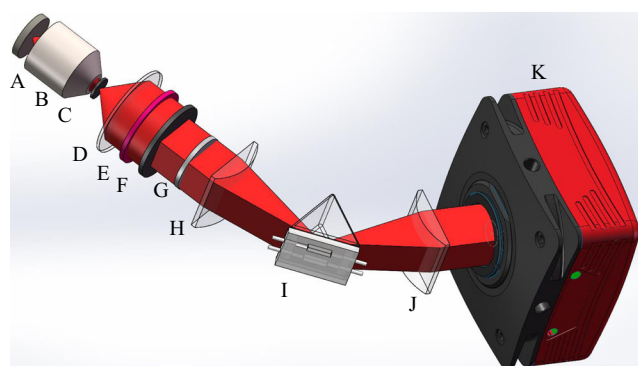

Fig. 3 Schematic of the experimental system setup. A Light-emitting diode, B objective lens, C pinhole, D convex lens, E bandpass filter, F linear glass polarizer, G rectangular aperture, H cylindrical lens, I SPR or WCSPR sensor module attached with a temperature-regulated fluidic system, J cylindrical lens, and K charge-coupled device

on thermal cycling principle was employed in this study for sample temperature configuration as described before [7, 40].

Results and Discussion

Static Measurement

The theoretical normalized angular reflectance spectra of SPR and WCSPR sensors were calculated based on multiple reflectance theory and Fresnel formula as shown in Fig. 4a. The distributions of electric field enhancement factor, which was defined as the intensity ratio of evanescent field to incident light, in SPR and WCPWR sensors were calculated and plotted against the distance from the prism surface based on transfer matrix approach as shown in Fig. 4b. Water ($n = 1.34$), the common solvent in the biochemical applications, was employed as the sample. The effect of Cr adhesive layer on the sensor performance was also taken into account. The numerical calculation method was described in detail before [39]. It can be seen from Fig. 4a that the theoretical predications showed that the WCSPR owns sharper resonance curve than SPR, which could provide easy determination of resonance angle position. It can be seen from Fig. 4b that although WCSPR sensor has stronger evanescent electric field, it owns the maximum evanescent electric field intensity at the film/water interface and short penetration depth of evanescent electric field as well as the SPR sensor. The evanescent electric field distribution characteristics of WCSPR are different from the PWR, which achieves the sharp resonance curve and evanescent electric field enhancement by increasing the
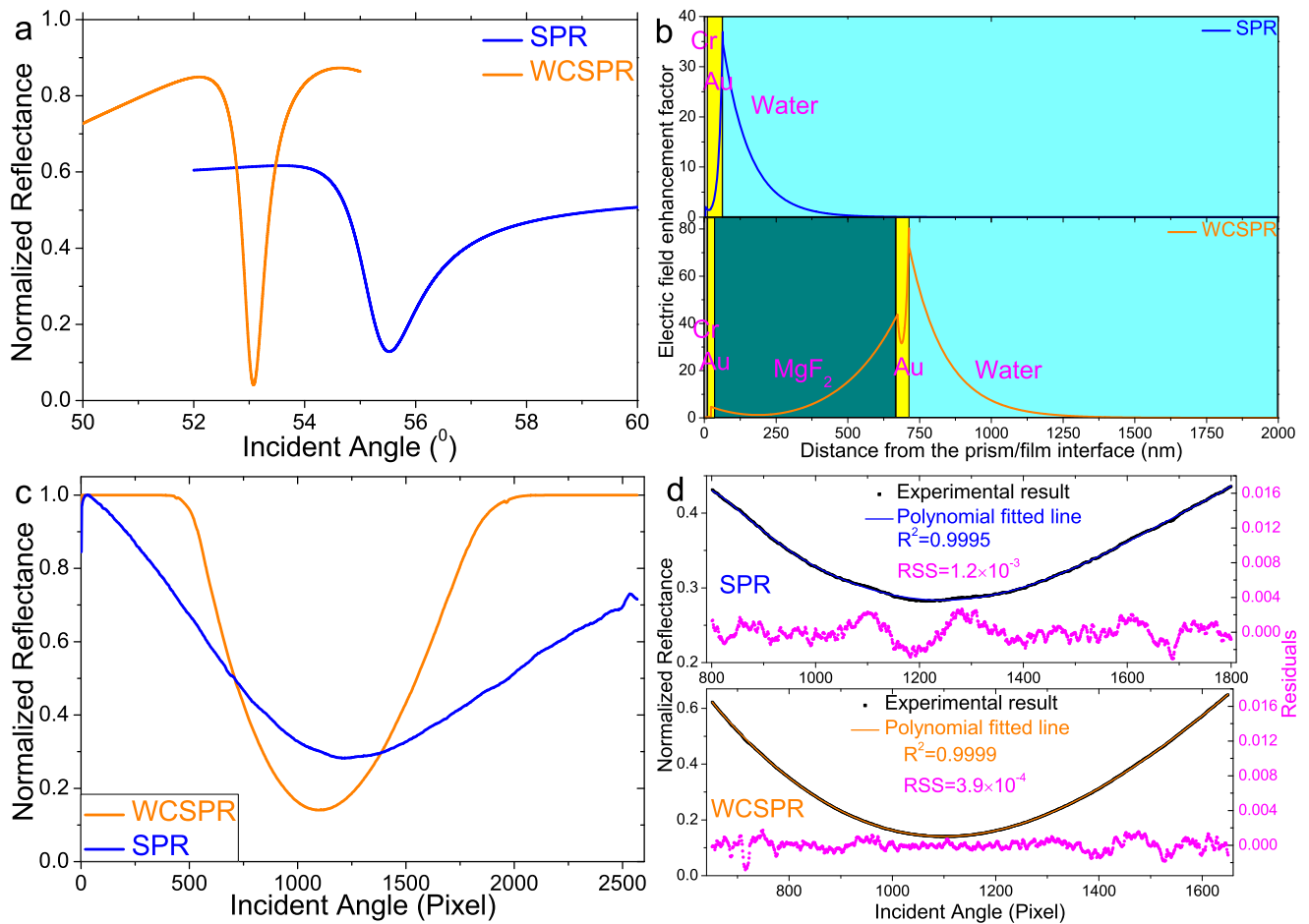
Fig. 4 **a** Normalized theoretical SPR and WCSPR reflectance spectra calculated by multiple reflectance theory and Fresnel formula with water as the sample. **b** Electric field enhancement factors of the SPR and WCSPR plotted against the distance from the prism surface. **c** Normalized experimental SPR and WCSPR reflectance spectra with water as the sample measured in the experiment. Different system angular resolutions and CCD positions were set for each sensor to achieve as whole resonance curve as possible with effective utilization of CCD sensing area. **d** Polynomial fitted results and corresponding residuals data of normalized experimental SPR, and WCSPR reflectance spectra. R^2 represented the determination coefficient, and RSS represented the residual sum of squares

interaction volume with sacrifice of surface sensing performance [41]. These indicate that the WCSPR may achieve better performances in both bulk and surface sensing applications than the conventional single-layered gold SPR.

The reflectance light beams of SPR and WCSPR sensors were captured by CCD, and one hundred rows were averaged to acquire the normalized experimental reflectance spectra as shown in Fig. 4c. The system angular resolution was adjusted to be higher for measuring the resonance curve of WCSPR than SPR, and the CCD was also adjusted to an appropriate position for each sensor to achieve as whole resonance curve as possible with effective utilization of CCD sensing area, which has been demonstrated to be benefit for the measurement quality [22]. The nine-order polynomial fitting was employed to determine the resonance angle represented by the corresponding pixel position affording the minimum intensity in the reflectance spectra. The polynomial fitting results and corresponding residual diagrams of normalized SPR,

and WCSPR reflectance spectra were shown in Fig. 4d. It can be seen that the WCSPR owns not only higher determination coefficient R^2 but also lower residual sum of squares (RSS), which indicates that more accurate resonance angle position can be provided by using the WCSPR instead of the SPR for sensing applications.

RI Test

The water and the glucose solutions with concentrations of 1, 2, 3, 4, 5, 6, and 7 g/L were measured serially to test the sensor characteristics in bulk sensing applications. The sample temperature is stabilized at 30 °C during the measurement period. Fifty images are captured for each sample and the capture time interval is 5 s.

The measured resonance angles as the function of time and averaged measured resonance angle as the function of RI are shown in Fig. 5a, b, respectively. The RI resolution σ was

usually employed to estimate the bulk sensing performance of SPR sensors, which can be shown as follows:

$$S_{\text{bulk}} = \frac{\partial \theta}{\partial n}, \sigma = \frac{\sigma_{\text{SO}}}{S_{\text{bulk}}} \tag{3}$$

where θ is the resonance angle, n is the sample RI, and σ_{so} is the standard deviation of sensor output [42]. The standard deviation of the baseline created by the deionized water, whose RI is free of evaporation effects, is shown in Fig. 5a, and the S_{bulk} is achieved by the linear fitting in Fig. 5b. Using these data, the SPR resolution of 6.44×10^{-6} RIU and WCSPR resolution of 9.26×10^{-7} RIU can be achieved as shown in Fig. 5b. It can be seen that the resolution of WCSPR sensor could provide almost seven times smaller than that of conventional single-layered gold SPR sensor. This indicates that the WCSPR could achieve the RI resolution enhancement comparable to the high-resolution PWR sensor [37, 43], and owns better RI resolution than more currently proposed WCSPR sensors [28, 30, 34]. Besides, the WCSPR sensing approach is one kind of chip strategies for resolution enhancement without varying the hardware and software of measurement instruments, so it can be easily combined with other methods of improving SPR sensor performance, such as enhancing the evanescent electric field [44], utilizing the incident light in infrared region [45, 46], fabricating bimetal layer [47], and combining with other resonance modes [48–50], for further resolution enhancement.

Biomolecular Interaction Analysis

The biomolecular interaction between protein A and human IgG was monitored to test the surface sensing performances of SPR and WCSPR sensors. The MPA and EDC/NHS solutions were used to prepare the surface chemical states for immobilizing the protein A receptors with the workflow described before [7]. The 100 μg/mL protein A solution was pumped into the detection channel to create the biorecognition layer, and the PBS$_{\text{BSA}}$ buffer was pumped into both detection and reference channels to block the nonspecific sites. Finally, 25 and 50 μg/mL IgG solutions were serially pumped into both the detection and reference channels for the label-free analysis of biomolecular interaction between protein A receptors and IgG analytes in real time. During the measurement process, the sample temperature was configured at 37 °C, namely the human body temperature. The specific absorption effect inside the fluidic channels, where the IgG analytes could be specifically absorbed by the protein A receptors in the detection channels and had no interactions with the BSA in both detection and reference channels, was schematized as shown in Fig. 6(a).

The time courses of referenced SPR and WCSPR resonance angle shifts measuring the IgG solutions were shown in Fig. 6(b). The referenced resonance angle shifts represented the difference values between the resonance angle shifts in detection and referenced channels. It could be seen that the interaction curve measured by WCSPR was smoother than that measured by SPR, which should be owing to the higher CSF provided by WCSPR than SPR for the surface sensing applications. For quantitative comparison, the referenced interaction curves were fitted to Langmuir isotherm adsorption model between receptors at a surface and analytes in solution, which was shown as follows:
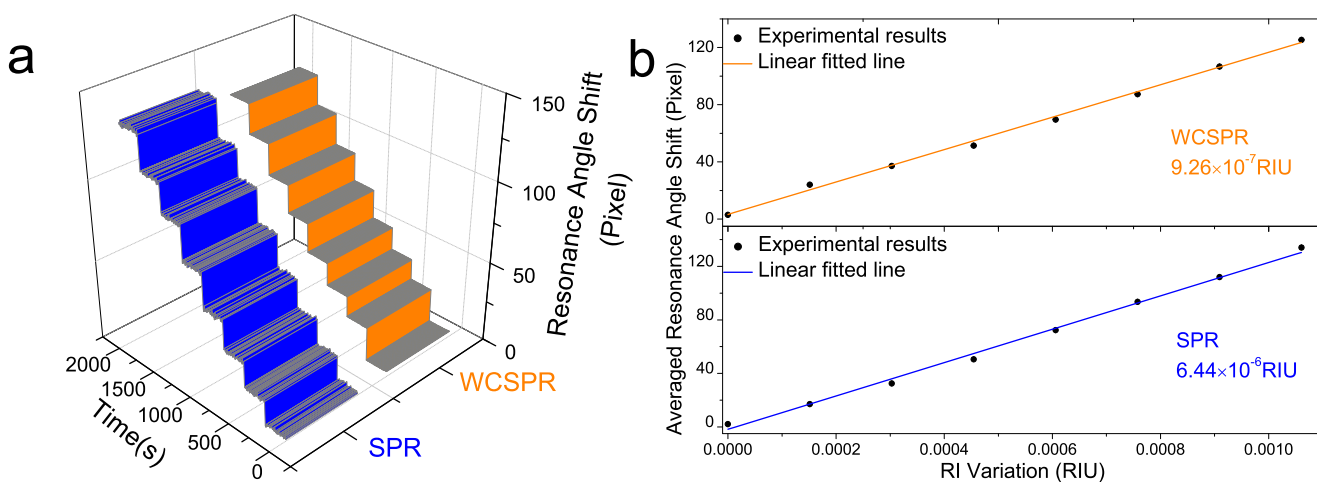
$$\text{Analyte} + \text{receptor} \underset{k_{\text{d}}}{\overset{k_{\text{a}}}{\rightleftharpoons}} \text{complex} \tag{4}$$

Fig. 5 a Measured resonance angle shift as function of time. b Averaged measured resonance angle shift as function of the RI variation. The error bars representing the standard errors lie within the data characters
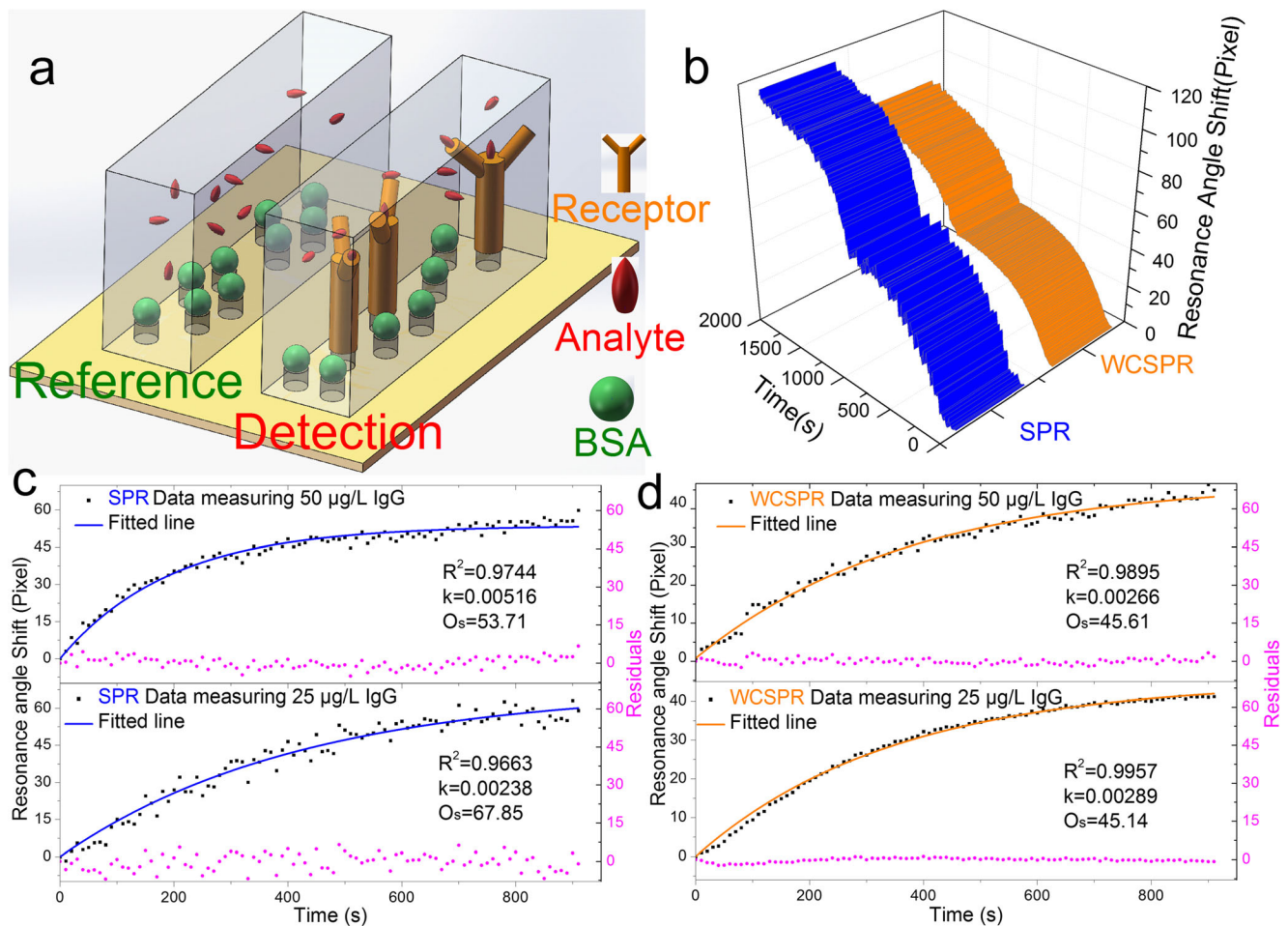
Fig. 6 (a) Schematic representations of specific molecular absorption on the sensing surface inside the fluidic channels. (b) Referenced SPR and WCSPR resonance angle shifts plotted against time measuring the IgG solution with concentrations of 25 and 50 μg/mL serially. (c, d) Time course of SPR, CLPWR resonance angle shifts, and corresponding fitting results measuring 25 μg/mL IgG solution as the PBS buffer was employed to create the baseline and 50 μg/mL IgG solution as 25 μg/mL IgG solution was employed to create the baseline

where k_a was association rate constant and k_d was dissociation rate constant. The amount of the complexes γ at time t could be expressed as follows:

$$\frac{d\gamma}{dt} = k_a \alpha_0 (\beta - \gamma) - k_d \gamma \quad (5)$$

where α_0 was the analyte concentration in solution and $\beta - \gamma$ was the instantaneous concentrations of the free receptors. For the label-free optical biosensors, the amount of the complexes γ could be indicated by the sensor output (O). Defining the initial time $t = 0$ and the baseline $O = 0$ for complex formation, after the integral operation, Eq. (5) could be expressed as follows:

$$O = O_S \left(1 - e^{-kt}\right) \quad (6)$$

where O_s was the sensor output at saturation stage and $k = k\alpha_0 + k_d$.

The time courses of referenced SPR and WCSPR resonance angle shifts measuring the IgG solutions were fitted to Eq. (6) and shown in Fig. 6(c, d), respectively. It could be seen that higher determination coefficient R^2, smaller residuals, and O_s values agreeing better with the experimental results were achieved by using the WCSPR instead of the SPR for biomolecular interaction analysis with the same workflow and experimental system. These could also be owing to the higher CSF provided by WCSPR than SPR for the surface sensing applications. Large difference of k compared with other cases appeared when the SPR sensor was employed to measure the specific molecular interaction between protein A receptors and IgG analytes with concentration of 50 μg/mL with using the 25 μg/mL IgG solution to create the baseline. This may be because that the molecular interaction included both the association and dissociation effects, and the competition between them became more intense along with the increase of IgG concentration. As known, the main advantage of label-free biosensors was that they can permit process monitoring of

molecular interaction in real time for dynamic analysis. This experiment demonstrated that the WCSPR sensor could provide more accurate and reliable measurement results for biomolecular interaction analysis. Therefore, the WCSPR was experimentally demonstrated to be able to provide better performance in surface sensing applications than the conventional single-layered gold SPR.

Conclusion

In this paper, we describe an Au-MgF$_2$-Au trilayered WCSPR sensing structure. It can be readily prepared with common vacuum film coating technique, and the theoretical calculation shows that it permits film thickness error within 15% of the targeted value. Owing to the coupling of SPR and waveguide modes, the WCSPR could achieve sharper resonance curve and stronger evanescent field than the conventional single-layered gold SPR, which make that the WCSPR could achieve seven times smaller RI resolution in the bulk sensing application and provide more accurate measurement results for the biomolecular interaction analysis. We believe that the WCSPR provide a simple and convenient chip-based strategy for performance enhancement of SPR sensors without varying the hardware and software of measurement instruments.

References

1. Homola J (2006) Surface plasmon resonance based sensors. Springer Berlin Heidelberg, New York
2. Shan XN, Patel U, Wang SP, Iglesias R, Tao NJ (2010) Imaging local electrochemical current via surface plasmon resonance. Science 327:1363–1366
3. Wong CL, Olivo M (2014) Surface plasmon resonance imaging sensors: a review. Plasmonics 9:809–824
4. Cooper MA (2009) Label-free biosensors: techniques and applications. Cambridge University Press, New York
5. Zijlstra P, Paulo PMR, Orrit M (2012) Optical detection of single non-absorbing molecules using the surface plasmon resonance of a gold nanorod. Nat Nanotechnol 7:379–382
6. Chong XY, Liu L, Liu ZY, Ma SH, Guo J, Ji YH, He YH (2013) Detect the hybridization of single-stranded DNA by parallel scan spectral surface plasmon resonance imaging. Plasmonics 8:1185–1191
7. Zhang PF, Liu L, He YH, Ji YH, Guo J, Ma H (2016) Temperature-regulated surface plasmon resonance imaging system for bioaffinity sensing. Plasmonics 11:771–779
8. Hinman SS, McKeating KS, Cheng Q (2018) Surface plasmon resonance: material and interface design for universal accessibility. Anal Chem 90:19–39
9. Liu L, Chen XL, Liu ZY, Ma SH, Du C, He YH, Guo JH (2012) Polarization interference interrogation of angular surface plasmon resonance sensors with wide metal film thickness tolerance. Sensors Actuators B Chem 173:218–224
10. Liu L, Guo J, He YH, Zhang PF, Zhang YL, Guo JH (2015) Study on the despeckle methods in angular surface plasmon resonance imaging sensors. Plasmonics 10:729–737
11. Chen ZL, Liu L, He YH, Ma H (2016) Resolution enhancement of surface plasmon resonance sensors with spectral interrogation: resonant wavelength considerations. Appl Opt 55:884–891
12. Luo L, Qiu XD, Xie LG, Liu X, Li ZX, Zhang ZY, Du JL (2017) Precision improvement of surface plasmon resonance sensors based on weak-value amplification. Opt Express 25:21107–21114
13. Wu B, Jiang R, Wang Q, Huang J, Yang XH, Wang KM, Li WS, Chen ND, Li Q (2016) Detection of C-reactive protein using nanoparticle-enhanced surface plasmon resonance using an aptamer-antibody sandwich assay. Chem Commun 52:3568–3571
14. Liu CJ, Hu FC, Yang W, Xu JY, Chen Y (2017) A critical review of advances in surface plasmon resonance imaging sensitivity. Trac-Trend Anal Chem 97:354–362
15. Kabashin AV, Evans P, Pastkovsky S, Hendren W, Wurtz GA, Atkinson R, Pollard R, Podolskiy VA, Zayats AV (2009) Plasmonic nanorod metamaterials for biosensing. Nat Mater 8:867–871
16. Chang CC, Chiu NF, Lin DS, Yu CS, Liang YH, Lin CW (2010) High-sensitivity detection of carbohydrate antigen 15-3 using a gold/zinc oxide thin film surface plasmon resonance-based biosensor. Anal Chem 82:1207–1212
17. Wang ZY, Cheng ZQ, Singh V, Zheng Z, Wang YM, Li SP, Song LS, Zhu JS (2014) Stable and sensitive silver surface plasmon resonance imaging sensor using trilayered metallic structures. Anal Chem 86:1430–1436
18. Yang CT, Mejard R, Griesser HJ, Bagnaninchi PO, Thierry B (2015) Cellular micromotion monitored by long-range surface plasmon resonance with optical fluctuation analysis. Anal Chem 87:1456–1461
19. Isaacs S, Abdulhalim I (2015) Long range surface plasmon resonance with ultra-high penetration depth for self-referenced sensing and ultra-low detection limit using diverging beam approach. Appl Phys Lett 106:193071
20. Kenakin TP (2009) Cellular assays as portals to seven-transmembrane receptor-based drug discovery. Nat Rev Drug Discov 8:617–626
21. Shi H, Liu ZY, Wang XX, Guo J, Liu L, Luo L, Guo JH, Ma H, Sun SQ, He YH (2013) A symmetrical optical waveguide based surface plasmon resonance biosensing system. Sensors Actuators B Chem 185:91–96
22. Zhang PF, Liu L, He YH, Shen ZY, Guo J, Ji YH, Ma H (2014) Non-scan and real-time multichannel angular surface plasmon resonance imaging method. Appl Opt 53:6037–6042
23. Lin H, Wang LP, Dong JX, Xu XY, Liu L, Zhang L, Huang Q, Zhang XH, Liu QQ (2015) Study on trace sample of chronic skin ulcer with a symmetrical optical waveguide-based surface plasmon resonance biosensor. Plasmonics 10:1631–1637
24. Zhang PF, Liu L, He YH, Zhou YF, Ji YH, Ma H (2015) Noninvasive and real-time plasmon waveguide resonance thermometry. Sensors 15:8481–8498
25. Wang GQ, Wang CJ, Sun SQ (2018) An optical waveguide sensor based on mesoporous silica films with a comparison to surface plasmon resonance sensors. Sensors Actuators B Chem 255:3400–3408
26. Ma TF, Chen YP, Guo JS, Wang W (2018) Cellular analysis and detection using surface plasmon resonance imaging. Trac-Trend Anal Chem 103:102–109
27. Grotewohl H, Hake B, Deutsch M (2016) Intensity and phase sensitivities in metal/dielectric thin film systems exhibiting the

coupling of surface plasmon and waveguide modes. Appl Opt 55: 8564–8570

28. Song LS, Wang ZY, Zhou DS, Nand A, Li SP, Guo BH, Wang YM, Cheng ZQ, Zhou WF, Zheng Z, Zhu JS (2013) Waveguide coupled surface plasmon resonance imaging measurement and high-throughput analysis of bio-interaction. Sensors Actuators B Chem 181:652–660

29. Ahn JH, Seong TY, Kim WM, Lee TS, Kim IH, Lee KS (2012) Fiber-optic waveguide coupled surface plasmon resonance sensor. Opt Express 20:21729–21738

30. Hayashi S, Nesterenko DV, Sekkat Z (2015) Waveguide-coupled surface plasmon resonance sensor structures: Fano lineshape engineering for ultrahigh-resolution sensing. J Phys D Appl Phys 48: 325303

31. Yang L, Wang JC, Yang LZ, Hu ZD, Wu XJ, Zheng GG (2018) Characteristics of multiple Fano resonances in waveguide-coupled surface plasmon resonance sensors based on waveguide theory. Sci Rep-UK 8:2560

32. Bera M, Ray M (2014) Angular piecewise modal analysis for waveguide-coupled surface plasmon resonance structure. J Lightwave Technol 32:3199–3205

33. Lee YK, Lee KS, Kim WM, Sohn YS (2014) Detection of amyloid-b42 using a waveguide-coupled bimetallic surface plasmon resonance sensor chip in the intensity measurement mode. PLoS One 9: e98992

34. Lee HS, Seong TY, Kim WM, Kim I, Hwang GW, Lee WS, Lee KS (2018) Enhanced resolution of a surface plasmon resonance sensor detecting C-reactive protein via a bimetallic waveguide-coupled mode approach. Sensors Actuators B Chem 266:311–317

35. Hsu SH, Lin JH, Tsai DZ, Tsai HS, Jian ZH, Liu HF (2016) MicroRNA biosensing using telecommunication wavelength-interrogated waveguide-coupled surface plasmon resonance. IEEE Sensors J 16:2890–2891

36. Twari K, Sharma SC, Hozhabri N (2016) Hafnium dioxide as a dielectric for highly-sensitive waveguide-coupled surface plasmon resonance sensors. AIP Adv 6:045217

37. Zhou YF, Zhang PF, He YH, Xu ZH, Liu L, Ji YH, Ma H (2014) Plasmon waveguide resonance sensor using an Au-MgF$_2$ structure. Appl Opt 53:6344–6350

38. Bahrami F, Maisonneuve M, Meunier M, Aitchison JS, Mojahedi M (2014) Self-referenced spectroscopy using plasmon waveguide resonance biosensor. Biomed Opt Express 5:2481–2487

39. Zhang PF, Liu L, He YH, Ji YH, Ma H (2015) Self-referenced plasmon waveguide resonance sensor using different waveguide modes. J Sens 2015:945908

40. Zhang PF, Liu L, He YH, Xu ZH, Ji YH, Ma H (2015) One-dimensional angular surface plasmon resonance imaging based array thermometer. Sensors Actuators B Chem 207:254–261

41. Abbas A, Linman MJ, Cheng Q (2011) Sensitivity comparison of surface plasmon resonance and plasmon-waveguide resonance biosensors. Sensors Actuators B Chem 156:169–175

42. Piliarik M, Homola J (2009) Surface plasmon resonance (SPR) sensors: approaching their limits? Opt Express 17:16505–16517

43. Sharma AK (2018) Simulation and analysis of Au-MgF2 structure in plasmonic sensor in near infrared spectral region. Opt Laser Technol 101:491–498

44. Zhang PF, Liu L, He YH, Chen XX, Ma KJ, Wei D, Wang H, Shao Q (2018) Composite layer based plasmon waveguide resonance for label-free biosensing with high figure of merit. Sensors Actuators B Chem 272:69–78

45. Pandey AK, Sharma AK, Basu R (2017) Fluoride glass-based surface plasmon resonance sensor in infrared region: performance evaluation. J Phys D Appl Phys 50:185103

46. Sharma AK, Dominic A (2018) Fluoride fiber-optic SPR sensor with graphene and NaF layers: analysis of accuracy, sensitivity, and specificity in near infrared. IEEE Sensors J 18:4053–4058

47. Sharma AK, Mohr GJ (2016) Plasmonic optical sensor for determination of refractive index of human skin tissues. Sensors Actuators B Chem 226:312–317

48. Abutoama M, Li SZ, Abdulhalim I (2017) Widening the spectral range of ultrahigh field enhancement by efficient coupling of localized to extended plasmons and cavity resonances in grating geometry. J Phys Chem C 121:27612–27623

49. Baaske MD, Foreman MR, Vollmer F (2014) Single-molecule nucleic acid interactions monitored on a label-free microcavity biosensor platform. Nat Nanotechnol 9:933–939

50. Kim E, Baaske MD, Vollmer F (2016) In situ observation of single-molecule surface reactions from low to high affinities. Adv Mater 28:9941–9948